Fan Noise Boundary Layer Ingestion Installation Effects for NOVA Aircraft Configuration

Romani, Gianluca; Ye, Qingqing; Avallone, Francesco; Ragni, Daniele; Casalino, Damiano

DOI
10.2514/6.2019-2429

Publication date
2019

Document Version
Final published version

Published in
25th AIAA/CEAS Aeroacoustics Conference

Citation (APA)
Romani, G., Ye, Q., Avallone, F., Ragni, D., & Casalino, D. (2019). Fan Noise Boundary Layer Ingestion Installation Effects for NOVA Aircraft Configuration. In *25th AIAA/CEAS Aeroacoustics Conference: 20-23 May 2019 Delft, The Netherlands* Article AIAA 2019-2429 American Institute of Aeronautics and Astronautics Inc. (AIAA). https://doi.org/10.2514/6.2019-2429

Aeroacoustics Conferences
20-23 May 2019, Delft, The Netherlands
25th AIAA/CEAS Aeroacoustics Conference

10.2514/6.2019-2429

Fan Noise Boundary Layer Ingestion Installation Effects for NOVA Aircraft Configuration

G. Romani[*], Q. Ye[†], F. Avallone[‡], D. Ragni[§], D. Casalino[¶]
Delft University of Technology, Kluyverweg 1, 2629HS, Delft, The Netherlands

Aim of this paper is to investigate the effects of the turbulent flow developing over a fuselage on fan noise for Boundary Layer Ingestion (BLI) embedded propulsion systems. Such engine configurations can suffer from inlet flow distortions and ingestion of turbulence at the fan plane with consequent impact on both broadband and tonal fan noise. The analysis is performed by considering a modified version of the Low-Noise configuration of the NASA Source Diagnostic Test (SDT) integrated into the Nextgen ONERA Versatile Aircraft (NOVA) fuselage in order to reproduce the NOVA BLI configuration. The numerical flow solution is obtained by solving the explicit, transient and compressible lattice-Boltzmann equation implemented in the high-fidelity CFD/CAA solver Simulia PowerFLOW®. The acoustic far-field is computed by using the Ffwocs-Williams & Hawkings integral solution applied to a permeable surface encompassing the fan-stage. Simulations are performed for an operating condition representative of a take-off with power cutback. Installation effects due to the BLI configuration are quantified by comparison with an isolated configuration of the modified Low-Noise SDT fan-stage geometry at same operating conditions. Comparisons are carried out in terms of fan-stage intake/interstage velocity fields, fan blades section air-loads and far-field noise; correlations between the fan-stage velocity field and noise emission for the BLI configuration are outlined. It is found that the BLI fan-stage is characterized by strong azimuthal fan blade loading unsteadiness, less periodic and coherent rotor wake tangential velocity variations and higher levels of in-plane velocity fluctuations compared to the isolated engine, resulting in far-field noise spectra with no distinct tonal components and higher broadband levels. This study represents the first high-fidelity CFD/CAA simulation of a full-scale aircraft geometry comprehensive of a BLI fan/Outlet Guide Vane (OGV) stage.

I. Introduction

In order to deal with the increasingly stringent aviation regulations for pollution and noise impact,[1] the use of Ultra-High Bypass Ratio (UHBR) engines on next generation aircraft is getting more consideration due to their lower jet core flow velocity and noise emissions, and enhanced propulsive efficiency compared to Low- and High-Bypass turbofans. Such engines have a larger fan diameter with consequent increase of the tip speed. As consequence of jet noise reduction, it is expected that fan noise becomes the primary source of noise for these configurations for most of the flight conditions.[2] Moreover, their actual employment on future aircraft raises new integration challenges, requiring special designs to install such large and heavy engines minimizing their impact on aircraft performances.

In the last two decades, many researchers have focused their efforts on developing novel aircraft configurations suited for UHBR engines integration.[3–6] In this scenario, four different NOVA (Nextgen ONERA Versatile Aircraft) aircraft geometries have been designed at ONERA in last few years with a particular emphasis on engine integration: (i) a baseline architecture with wide lifting fuselage, under-wing engines, high wing aspect ratio and downward oriented winglets, (ii) a gull wing layout characterized by an increased

---

[*] PhD Candidate, AWEP Department, AIAA member, `G.Romani@tudelft.nl`
[†] Postdoctoral Research Associate, AWEP Department, AIAA member, `Q.Ye-1@tudelft.nl`
[‡] Assistant Professor, AWEP Department, AIAA member, `F.Avallone@tudelft.nl`
[§] Assistant Professor, AWEP Department, AIAA member, `D.Ragni@tudelft.nl`
[¶] Professor of Aeroacoustics, AWEP Department, AIAA member, `D.Casalino@tudelft.nl`

dihedral angle in the wing inboard position to limit landing gears length, (iii) a podded configuration with engines mounted on the aft fuselage side, and (iv) a Boundary Layer Ingestion (BLI) configuration with engines installed on the aft fuselage side and ingesting the boundary layer convecting over the fuselage.[5] Starting from these studies, the present work, which takes place in the framework of the European Commission project ARTEM (Aircraft noise Reduction Technologies and related Environmental iMpact), focuses on the latter configuration. BLI propulsion systems aim at reducing mass and drag penalty as well as jet and wake losses compared to conventional configurations,[5–8] thus leading to a potential reduction of the required propulsive power. However, many drawbacks should be addressed before quantifying the actual benefits associated to BLI, such as the inlet flow distortion on engine efficiency, operability, aeromechanics and aeroacoustics. The fuselage boundary layer ingestion, as well as the possible presence of a s-duct inlet, lead to the partial loss of the fan inflow axial uniformity thus causing a strong azimuthal variation of the fan blade loading with either aerodynamic or aeroacoustic drawbacks. Therefore, this kind of engine integration deeply relies upon the possibility to alleviate the flow distortion and non-uniformity at the fan plane.

Although an extensive research has been conducted in order to investigate BLI propulsion systems in terms of performances and fuel efficiency,[7,9–14] and inlet inflow assessment,[15–17] only few aeroacoustic studies are available in literature for such configurations. Defoe *et al.*[18] have investigated the effects of BLI on the aeroacoustics of transonic fan rotors, by implementing a body-force formulation for the fan rotor description, extracted from a 3D Reynolds-Averaged Navier-Stokes (RANS) simulation, in an unsteady Euler calculation and evaluating the far-field noise via the Ffowcs-Williams and Hawkings integral method using a permeable surface. They found that the dominant mechanism for changes in far-field rotor shock noise due to the boundary layer ingestion at low free-stream Mach numbers is the ingestion of stream-wise vorticity. A noise assessment at aircraft-level for the NASA D8 concept has been carried out by Clark *et al.*[19] by using the Aircraft NOise Prediction Program (ANOPP) comprehensive tool to predict the noise generated by each source component, with the BLI influence on fan noise empirically modeled with experimental data. In that study, boundary layer ingestion was predicted to have a detrimental impact on effective perceived noise levels in the order of 15 dB. Finally, Murray *et al.*[20] conducted aeroacoustic measurements for an unshrouded rotor partially immersed in a turbulent boundary layer at low Mach number to investigate inflow distortion effects associated to airframe-integrated engines. They found that, at low and moderate thrust conditions, the rotor produces broadband noise organized into haystacks generated by large eddies of ingested turbulence being cut multiple times by neighboring rotor blades, contrarily to louder and more tonal acoustic signatures observed at high thrust condition. Since there are no detailed studies on the physics behind the noise generation for BLI embedded engines at both component and full-aircraft levels, the aim of this paper is twofold: (i) to perform the first, to the authors' knowledge, high-fidelity CFD/CAA simulation of a full-scale aircraft geometry comprehensive of a BLI fan/Outlet Guide Vane (OGV) stage and (ii) to address BLI installation effects on fan noise for a NOVA BLI-like configuration.

In this paper, Simulia's PowerFLOW® time-explicit, compressible and transient solver based on the Lattice-Boltzmann Method/Very Large Eddy Simulation (LBM/VLES) is used to simulate and analyze the flow and the acoustics near field around the BLI fan stage. The aerodynamic noise generated by the fan blade, the fan wake/OGV interaction and the interaction with the ingested turbulence is then estimated by using an acoustic analogy based on the Ffowcs-Williams and Hawkings (FW-H) equation. The same methodology and a similar computational setup have been already used and successfully validated in the past by several authors[21–23] to predict fan tonal and broadband noise of three fan/OGV configurations of the 22-in NASA Source Diagnostic Test (SDT) fan rig[24] at both subsonic and transonic tip speed conditions.

The manuscript is organized as follows. In Sec. II, an overview the LBM/VLES approach is presented. The fan-stage configurations and the computational setup are described in Sec. III. Aerodynamic and aeroacoustic installation effects associated to the NOVA BLI configuration are discussed in Sec. IV. Finally, the main conclusions and future outlook of this study are drawn in Sec. V.

II. Numerical Method

II.A. LBM-VLES flow solver

The LBM core of the CFD/CAA solver PowerFLOW® solves the Boltzmann equation for the distribution function $f(\mathbf{x}, t, \mathbf{v})$ on a hexahedral mesh automatically generated around bodies, which consist of one or more connected solid parts. The function f represents the probability to find, in the elementary volume $d\mathbf{x}$ around $\mathbf{x}$ and in the infinitesimal time interval $(t, t + dt)$, a number of fluid particles with velocity in the interval $(\mathbf{v}, \mathbf{v} + d\mathbf{v})$. The Boltzmann equation is solved by discretizing the space velocity domain into a prescribed number of values in magnitude and direction. These discrete velocity vectors are such that, in a prescribed time step, one particle can be advected from one point of the mesh to N neighboring points, including the point itself. In this study, an hybrid formulation of the solver is used, which allows to combine 19 (D3Q19) and 39 (D3Q39) particle velocity states, the latter being used where transonic flow is expected.[25] The standard LBM formulation is based on the time-explicit advection equation:

$$f_i(\mathbf{x} + \mathbf{v}_i\Delta t, t + \Delta t) - f_i(\mathbf{x}, t) = C_i(\mathbf{x}, t), \tag{1}$$

where f_i represents the particle distribution function along the i-th direction, according to the finite set of discrete velocities $\mathbf{v}_i$, and $\mathbf{v}_i\Delta t$ and Δt are the space and time increments, respectively. The left-hand side of Eq. 1 corresponds to the particle advection, while the right-hand side is the collision operator, which represents the rate of change of f_i resulting from collision (i.e. the interaction of particles). The collision term C_i is modeled with the well-known Bhatnagar-Gross-Krook (BGK) approximation:[26, 27]

$$C_i(\mathbf{x}, t) = -\Delta t/\tau[f_i(\mathbf{x}, t) - f_i^{eq}(\mathbf{x}, t)], \tag{2}$$

where τ is the relaxation time parameter, which is related to the fluid dimensionless kinematic viscosity ν and temperature T according to $\tau = \nu/T + \Delta t/2$, and f_i^{eq} is the equilibrium distribution function, which is related to local hydrodynamic properties.[28] For compressible flows, the LBM is coupled with an entropy partial differential equation to satisfy the conservation of energy (non isothermal model).[25] Once the distribution function is computed, hydrodynamic flow quantities, such as flow density, velocity and temperature, can be determined through discrete integration of the distribution function f_i, respectively:

$$\rho(\mathbf{x}, t) = \sum_i f_i(\mathbf{x}, t), \quad \rho\mathbf{u}(\mathbf{x}, t) = \sum_i f_i(\mathbf{x}, t)\mathbf{v}_i, \quad \rho e = \frac{D}{2}T = \sum_i f_i(\mathbf{x}, t)|\mathbf{v}_i - \mathbf{u}|^2 \tag{3}$$

with e the internal energy and $D = 3$ the spatial dimension. All the other physical quantities can be determined through thermodynamic relationships for an ideal gas.

For high Reynolds flows, turbulence modeling is introduced[29] into the LBM scheme by solving a variant of the renormalization group (RNG) $k - \epsilon$ model[30, 31] on the unresolved scales,[32] selected via a swirl model.[33] In particular, the two-equations based $k - \epsilon$ RNG model is used to compute a turbulent relaxation time that is added to the viscous relaxation time. This approach is referred to as LBM/Very Large Eddy Simulation (LBM/VLES).

Because resolving the wall boundary layer by using a Cartesian mesh approach down to the viscous sub-layer in high Reynolds number applications is prohibitively expensive, a wall function approach is used in PowerFLOW® to model boundary layers on solid surfaces. The wall function model is an extension of the standard law-of-the-wall formulation[34] to include the effects of favorable and adverse pressure gradients.[32]

The LBM scheme is solved on a grid composed of cubic volumetric elements (Voxels), the lattice, which is automatically created by the code. Different Variable Resolution (VR) regions can be defined by the user within the fluid domain in order to increase the volume discretization in regions of interest or where high flow gradients are expected. Being a Cartesian mesh used by the solver, a variable grid resolution by a factor of two is allowed between two adjacent VRs. Moreover, since the solver uses an explicit time-marching scheme based on a unitary Courant-Friedrichs-Lewy condition (i.e. CFL $= |max(\mathbf{v}_i)\Delta t|/\Delta x = 1$), the time step is also varied (and automatically defined by the code according to the voxel size of a certain VR region Δx and the discrete particle velocities $\mathbf{v}_i$) by a factor of two between two adjacent VRs. Therefore, the solution in coarser VRs is updated at a lower rate compared to finer VRs, and a balanced domain decomposition based on the equivalent number of voxels updated at every time step (i.e. Fine Equivalent Voxels, FEV) allows a tremendous speed-up of the transient flow simulation. The surface of solid bodies is automatically facetized within each voxel intersecting the wall geometry using planar surface elements (Surfels). For the no-slip and slip wall boundary conditions at each of these elements, a boundary scheme[35] is implemented, based on a particle bounce-back process and a specular reflection process, respectively. Therefore, very complex arbitrary geometries can be treated automatically by the LBM solver, simplifying the tedious manual work typically associated with the volume meshing step using other CFD approaches.

II.B. Noise computations

The CAA properties of LBM allow to analyze the acoustic near-field directly extracted from the transient flow solution. Due to the fact that the LBM is compressible and provides an unsteady solution, along with its low dissipation and dispersion properties, it is intrinsically suited for aeroacoustic simulations and allows to extract the sound pressure field directly in the near-field. In this work, both direct noise computations and FW-H far-field computations are performed. The employed FW-H solver is based on a forward-time solution[36] of Farassat's formulation 1A[37] extended to a permeable (porous) integration surface. The necessity to accurately capture the near-field noise propagation from the source region up to the FW-H integration surface is a requirement that can take advantage of the intrinsic lower dissipation and low-dispersion properties of the LBM scheme compared to partial differential equation discretization schemes. The FW-H code used in this work is part of Simulia's post-processing software PowerACOUSTICS® 4.1, which is also used to perform statistical and spectral analysis of any unsteady solution generated by PowerFLOW®.

III. Fan-stage Configurations and Computational Setup

III.A. Geometries and Operating Conditions

The geometry considered in this study is the NOVA lifting fuselage, wing and empennage (without engine and s-duct) - courtesy of ONERA - with a total length of 44 m and a semi-span of about 19 m. A modified version of the Low-Noise configuration of the NASA SDT, an existing scaled fan stage configuration publicly available in the framework of the AIAA Fan Broadband Noise Prediction Workshop,[24] was integrated into the fuselage to reproduce the NOVA BLI layout, as sketched in Figs. 1(a) and 1(b). In particular, the original Low-Noise SDT configuration, consisting of a 22-bladed fan and 26 stator swept vanes, was firstly scaled by a factor of 3.87689 to match the NOVA fan radius ($R = 1.075$ m) and equipped with a redesigned nacelle, obtained by increasing the original intake axial length in order to match the NOVA BLI engine intake-fan distance (2.35 m). A sketch of the modified Low-Noise SDT engine is depicted in Fig. 1(c). This redesigned engine geometry was then installed into the NOVA fuselage by considering a 40% buried intake, as in the original NOVA BLI layout, and tilt and toe angles of 1° and 2.5°, respectively. Finally, a s-shaped duct was designed to integrate the fan stage into the NOVA fuselage geometry, as shown in Fig. 1(d). Since the primary goal of this study is to address the fan noise impact for a NOVA BLI-like layout, two different configurations are investigated: (i) the isolated SDT fan/OGV stage with the modified nacelle (Fig. 1(c)) and (ii) the installed SDT fan/OGV stage into the original NOVA fuselage geometry (Fig. 1(d)).

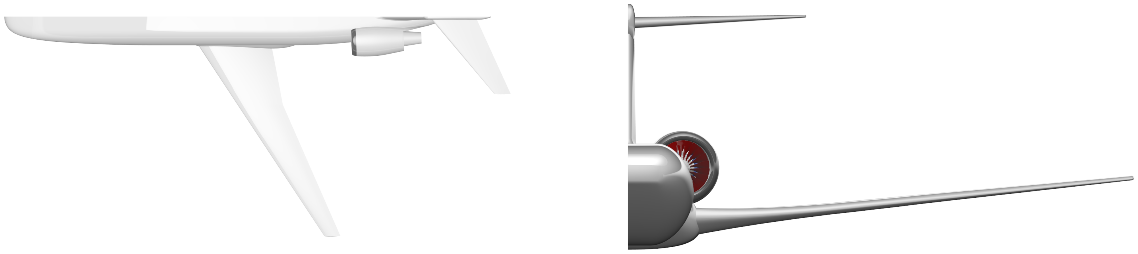

(a) *top view* (b) *front view*

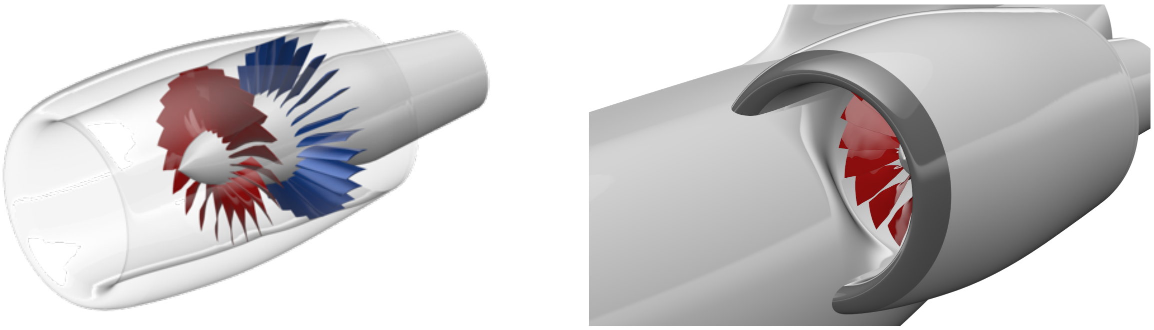

(c) *SDT fan stage with modified nacelle* (d) *SDT fan stage integration into NOVA fuselage*

Figure 1. NOVA aircraft configuration equipped with the redesigned BLI engine nacelle.

The operating conditions are representative of a take-off with power cutback. The free-stream Mach number is 0.25 and the static pressure (97718 Pa) and temperature (286.15 K) are taken from the International Standard Atmosphere (ISA) at 1000 ft. The aircraft angle of attack is 4°, the latter being considered for the isolated case as well (which also includes tilt and toe angles). Moreover, the fan angular velocity is 2602.71 RPM, corresponding to the 80% of SDT fan nominal power and resulting into a tip Mach number and a Blade-Passing Frequency (BPF) of 0.8680 and 954 Hz, respectively.

III.B. Computational Setup

Figure 2 depicts some details of the computational setup used in this study. The rotor and the spinner are encompassed by a volume of revolution that defines the Local Reference Frame (LRF), i.e. the rotating sliding mesh region used to reproduce the fan rotation. Since no primary jet was considered in this study, the center-body geometry is extended by employing an infinite solid cylinder downstream with slip boundary conditions to avoid flow recirculation behind it. For the BLI configuration, a zig-zag trip of 3.5 cm height, 5.8 cm wavelength and 6.4 cm amplitude was placed $3R$ upstream the engine inlet in order to trigger transition and ensure the ingestion of a turbulent boundary layer into the fan stage, while keeping the computational effort relatively low. The Ffowcs-Williams and Hawkings (FW-H) integration surface (depicted in Fig. 2 for both BLI and isolated configurations) used to compute the acoustic far-field consists of two regions: a spherical sector around the intake, and a conical surface in the exhaust region. The center part of the FW-H surface (cylinder) crosses through the solid walls of the nacelle: therefore, no flow data is extracted from there. The downstream cup of the cone is not included, in order to avoid noise contamination due to the hydrodynamic pressure fluctuations in the wake of the fan. However, the FW-H cone extends downstream enough to recover the by-pass exhaust radiation for the directivity angles of interest.

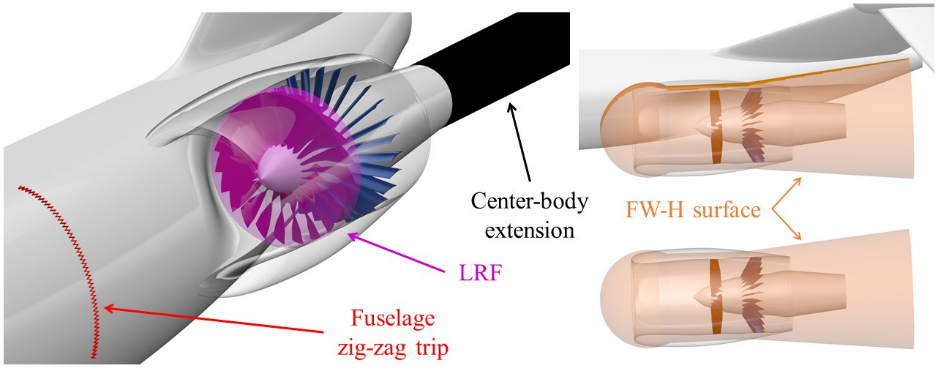

Figure 2. Details of the computational setup: LRF, transition trip, center-body extension and FW-H surface.

A cubic simulation volume of edge length of $690R$ centered around the engine is used. Free-stream static pressure and velocity are prescribed on the outer boundary, and an acoustic sponge approach is used to damp the out-going acoustic waves and minimize the backward reflection from the outer boundary. The acoustic sponge is defined by two concentric spheres of radius $40R$ and $150R$, respectively, and centered around the engine geometry. Hence, the fluid kinematic viscosity is gradually increased starting from its real value within the inner sphere, up to an artificial value two orders of magnitude higher outside the outer one. A total of 16 VR levels are employed to discretize the whole computational domain. The finest VR region covers the volume between the fan blade tip and the nacelle casing. The second finest VR level is used to discretize leading- and trailing-edges of both fan and OGV vanes. The third finest VR level is set as offset of fan, OGV and the nacelle bypass lip. The fourth finest VR level covers the whole bypass duct and the fuselage surface upstream the intake (for the installed case). The fifth finest VR level encloses the permeable surface used for FW-H computations. Finally all the other VRs, characterized by fuselage and/or engine offsets and boxes, are used to model the remaining part of the computational domain up to its boundaries. The grid resolution employed in this study is based on the *medium* resolution validated against the NASA SDT benchmark by Gonzalez-Martino and Casalino.[23] Such a resolution level results in a finest voxel size of 0.355 mm and roughly 6 voxels along the fan tip gap for the present computational setup. Simulations are performed using a 1000 cores cluster with Intel Xeon CPU E5-2697 2.6 GHz and require approximately

6 hours per fan revolution for both isolated and BLI cases. A summary of the grid size and computational cost for both installed and isolated cases are reported in Tab. 1.

The whole fluid domain is firstly initialized with a uniform stream-wise velocity corresponding to the free-stream conditions for a *coarse* simulation ($\sqrt{2}$ times coarser than the *medium* one), which is in turn used to initialize the *medium* resolution case. Hence, after a transient of 2 fan revolutions, corresponding to 0.0461 sec of physical time, sampling is started. Acoustic data are sampled at 180 kHz along 10 fan revolutions (0.2305 sec). Fourier transformed data are evaluated using a bandwidth of 25 Hz, 50% window overlap coefficient and Hanning weighting.

Table 1. Grid size in million of elements and computational cost (*medium* case).

Case	# Voxels	# FEVoxels	# Surfels	kCPUh (10 revs)
Isolated engine	541.1	69.6	51.9	61.5
BLI engine	545.9	70.1	57.5	62.1

IV. Numerical Results

In this section, the numerical results for both BLI and isolated fan-stage configurations are presented. First, a qualitative assessment of the fuselage turbulent boundary layer ingested by the engine for the installed case is briefly presented. Then, BLI installation effects are outlined in terms of fan-stage velocity field, fan blade section air-loads, far-field noise directivity and noise power levels.

IV.A. Fuselage Boundary Layer

As mentioned, a zig-zag transition trip is employed in this study to trigger transition of the fuselage boundary layer being ingested by the fan-stage. According to Van der Velden *et al*,[38] a canonical fully turbulent boundary layer is experienced for a zig-zag trip after approximately 40 laminar boundary layer thicknesses (evaluated at the location of the transition device) downstream the transition trip. Following this study, and considering the actual laminar boundary layer thickness evaluated at the transition trip location, a minimum settling trip-engine distance of $1R$ would be required to ensure the ingestion of a fully turbulent boundary layer into the fan-stage. Starting from these considerations, a larger and more conservative trip-engine distance of $3R$ was used. An instantaneous view of the stream-wise velocity component on a plane normal to the fuselage and passing through the engine axis is depicted in Fig. 3.

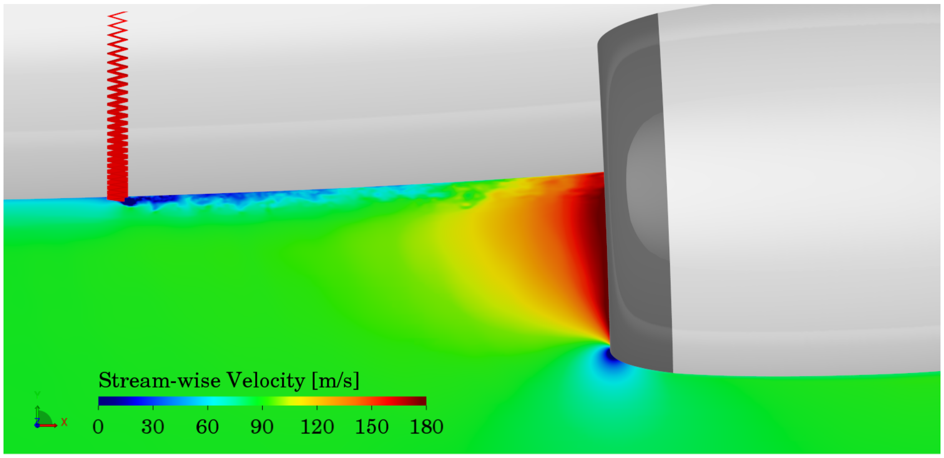

Figure 3. Instantaneous stream-wise velocity field past the transition trip on a plane normal to the fuselage and passing through the engine axis.

This result qualitatively shows the presence of a turbulent boundary layer convecting over the fuselage past the transition trip and being ingested by the fan-stage. Moreover, the thinning of the boundary layer and the stretch of turbulent structures into thin filaments are further observed as the flow approaches the fan-stage due to the large flow acceleration occurring across the engine inlet.

IV.B. Fan-Stage Velocity Field

Figure 4 depicts a schematic description of a plane normal to the fuselage and passing through the engine axis, and different cross-flow planes along the intake and interstage sections, which are used in the following sections to present the fan-stage velocity fields. In this schematization, the coordinate x (positive downstream and with origin on the fan center) denotes the position of the cross-flow planes along the engine axis.

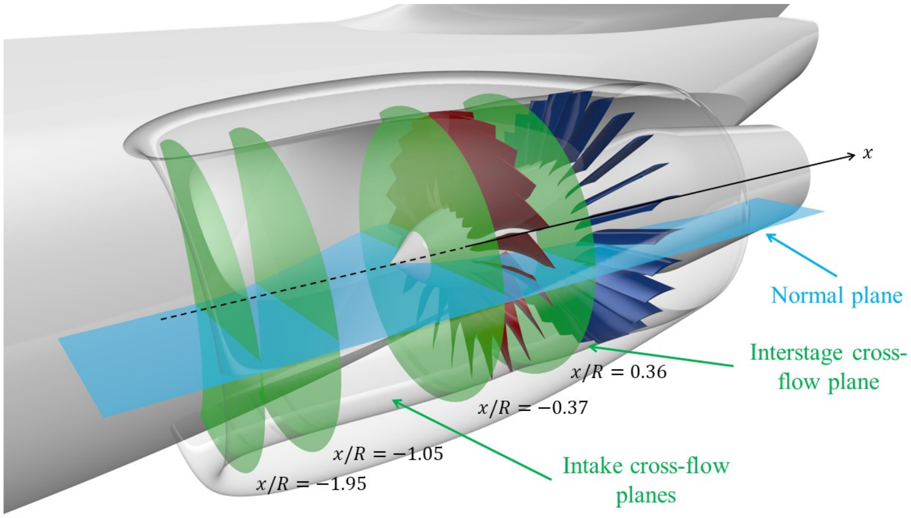

Figure 4. Schematic description of the planes used to extract the fan-stage velocity field. The coordinate x, positive downstream and with origin on the fan center, denotes the position along the engine axis.

Figure 5 show the instantaneous axial velocity field for the BLI case extracted on a plane normal to the fuselage surface and passing through the engine axis at different time instants. The same quantity is depicted on the same plane for the isolated case in Fig. 6. The BLI fan-stage shows a flow acceleration at the intake lip, due to the reduced inlet throat area of the installed configuration compared to the isolated one, and the presence of turbulence impinging the fan rotor on the fuselage side. Such turbulent structures are connected to the fuselage turbulent boundary layer ingested by the fan-stage, as well as to the flow separation occurring at approximately 60% of the s-duct length, the latter induced by the adverse pressure gradient and due to the rapid increase of the intake cross-sectional area. Conversely, the isolated configuration shows a rather uniform velocity field upstream the fan rotor, except for the first 25% of its extension, in which the flow tends to recovers from its initial misalignment with the axis engine due to the presence of non-zero angle of attack and tilt and toe angles. Upstream traveling waves are observed along the intake for the BLI engine, unlike to the isolated one. The BLI configuration shows a thicker boundary layer on the intake wall opposite to the fuselage compared to the isolated case, which also tends to separate in proximity of the fan plane. The instantaneous axial velocity field further shows the occurrence of two different fan wake/OGV interaction mechanisms between the fuselage and the nacelle sides for the BLI case, whereas the isolated case shows the typical rotor-stator interaction mechanism with the fan viscous wakes impinging on each stator vanes at the blade-passing frequency. The BLI configuration shows an unbalanced velocity field between the rotor and the stator, with much higher velocities observed in the region opposite to the fuselage side with respect to the isolated one. On this same region, the BLI case further shows stronger turbulent structures than those convecting along the fuselage side. Similar considerations can also be made for the fluid regions downstream the stator.

IV.B.1. Intake Flow Field

Figures 7 and 8 show the time-averaged axial, tangential and radial velocity components on cross-flow disks upstream the fan plane for the BLI and isolated configurations, respectively. In this upstream-looking-downstream view the fan blades rotate counter-clockwise as indicated by the black circular arrow. Three

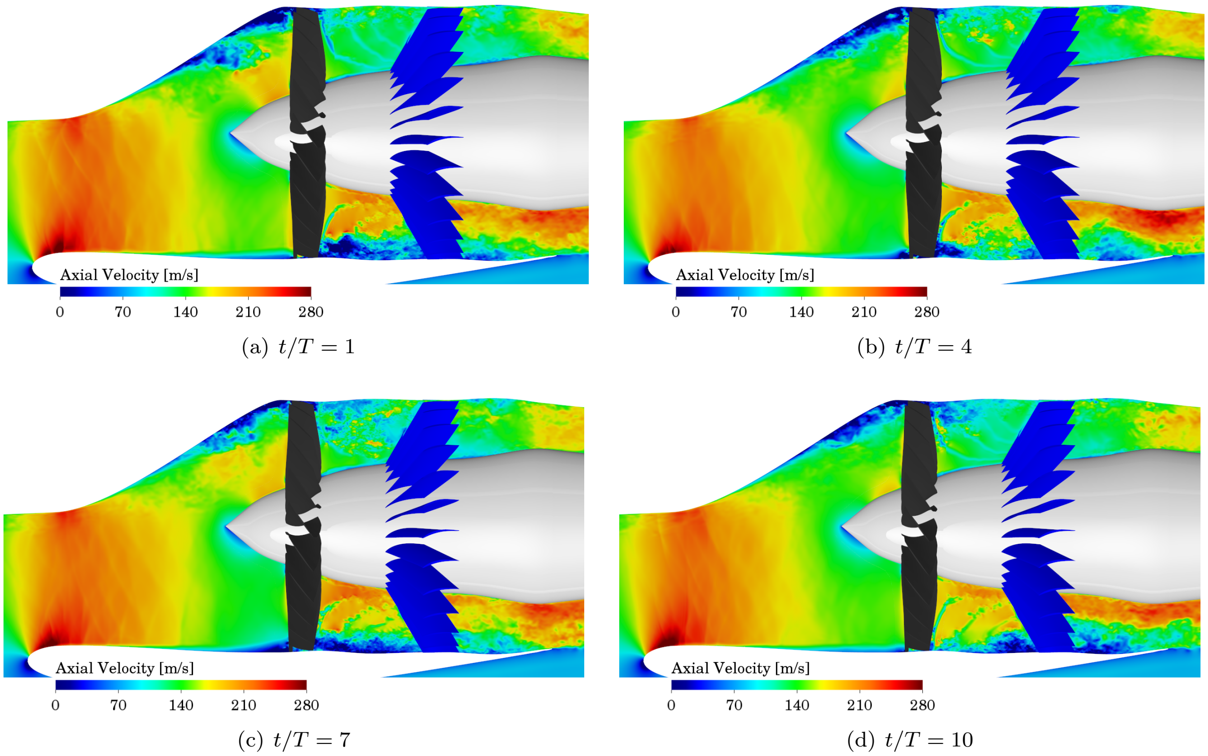

(a) $t/T = 1$ (b) $t/T = 4$ (c) $t/T = 7$ (d) $t/T = 10$

Figure 5. Instantaneous axial velocity field on a plane normal to the fuselage surface and passing through the engine axis for different time instants, BLI engine.

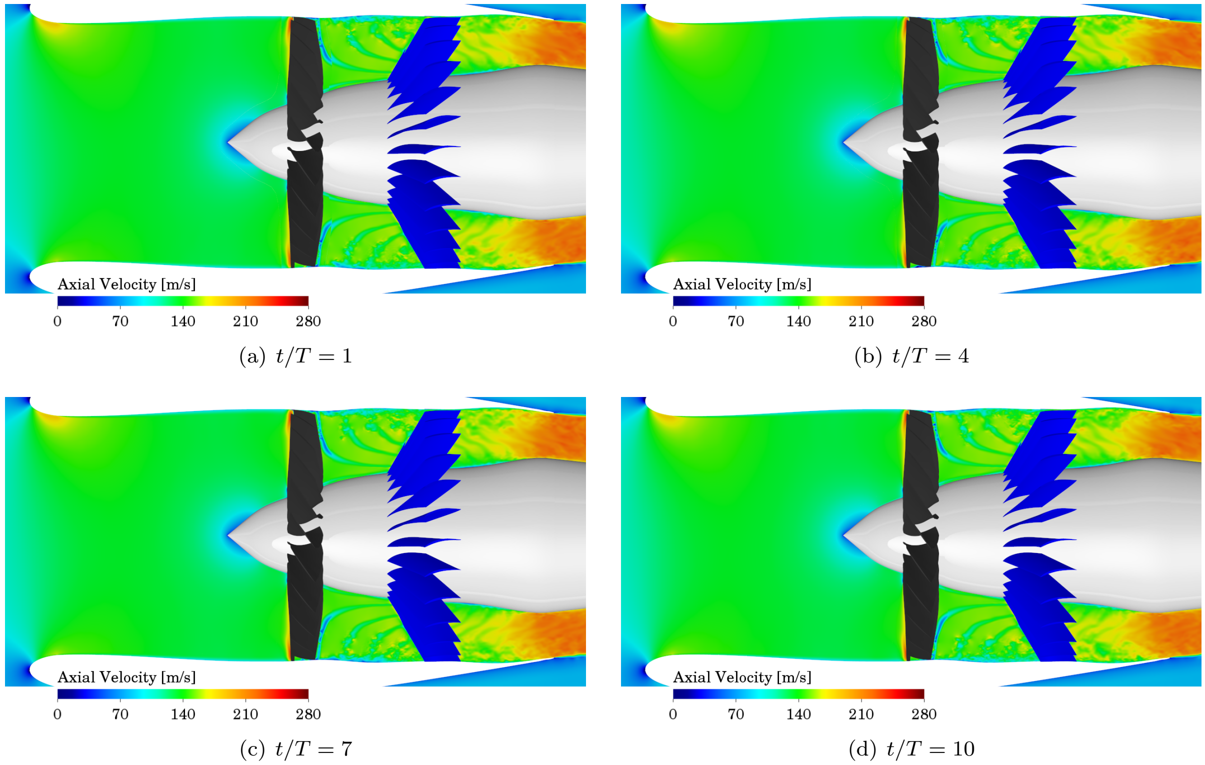

(a) $t/T = 1$ (b) $t/T = 4$ (c) $t/T = 7$ (d) $t/T = 10$

Figure 6. Instantaneous axial velocity field on a plane normal to the fuselage surface and passing through the engine axis for different time instants, isolated engine.

different stream-wise locations (i.e. $x/R = -1.95$, $x/R = -1.05$ and $x/R = -0.37$), respectively corresponding to 15%, 55% and 85% of the intake axial length, are considered. It should be mentioned that the tangential and radial velocities hereby considered are positive when directed in the direction of the fan rotation and for increasing radius, respectively. Moreover, the convention adopted to describe the fan blade azimuth angle is also reported. According to this convention, the BLI circular sector is approximately that for fan blade azimuth angles comprised between 45° and 180° (Fig. 8).

The isolated case shows a moderate level of distortion in proximity of the engine inlet, where the free-stream misalignment with the engine axis (due to the non-zero angle of attack, and tilt and toe angles) is responsible of the non-symmetric acceleration of the flow around the intake lip (Fig. 7(a)) and of the arise of a radial velocity component directed inboard (Fig. 7(c)). The azimuthal velocity field uniformity is then completely re-established within the first half of the intake extension, where the flow approaching the fan section shows a quite constant mean axial velocity (Figs. 7(d) and 7(g)) and a moderate radial velocity directed outboard, consequence of the slightly divergent intake geometry (Fig. 7(f)) and of the presence of the spinner downstream (Fig. 7(i)). Finally, the tangential velocity component turns out to be almost negligible for each intake section considered (Figs. 7(b), 7(e) and 7(h)).

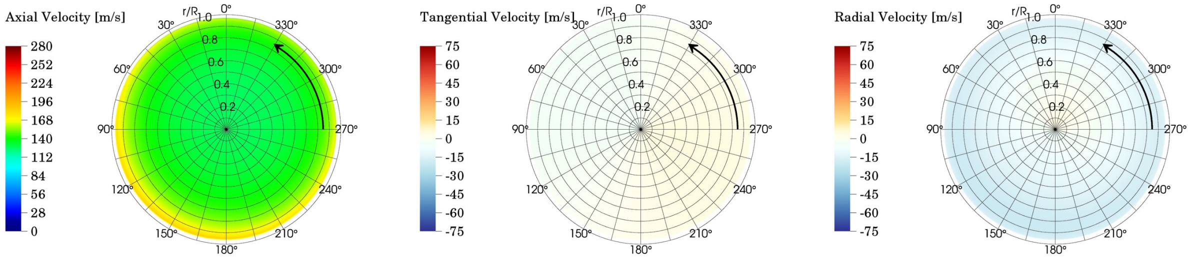

(a) *Axial component - x/R = -1.95* (b) *Tangential component - x/R = -1.95* (c) *Radial component - x/R = -1.95*

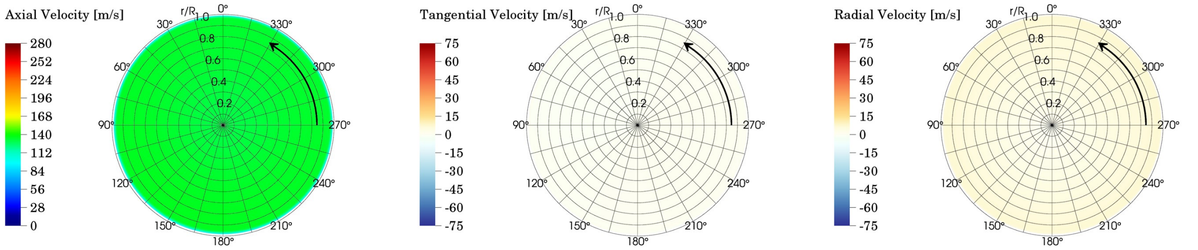

(d) *Axial component - x/R = -1.05* (e) *Tangential component - x/R = -1.05* (f) *Radial component - x/R = -1.05*

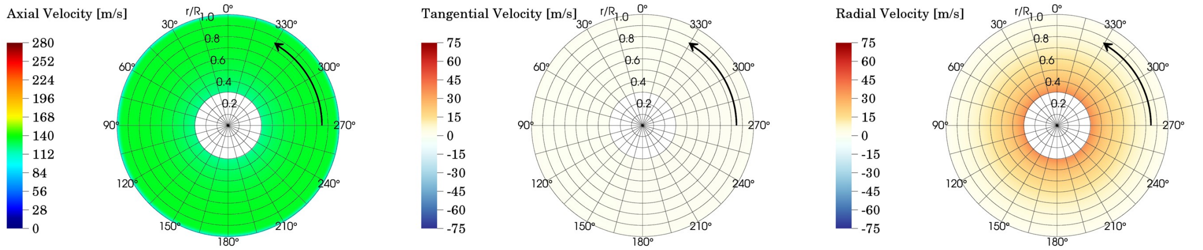

(g) *Axial component - x/R = -0.37* (h) *Tangential component - x/R = -0.37* (i) *Radial component - x/R = -0.37*

Figure 7. Time-averaged velocity field at different section upstream the fan, isolated engine.

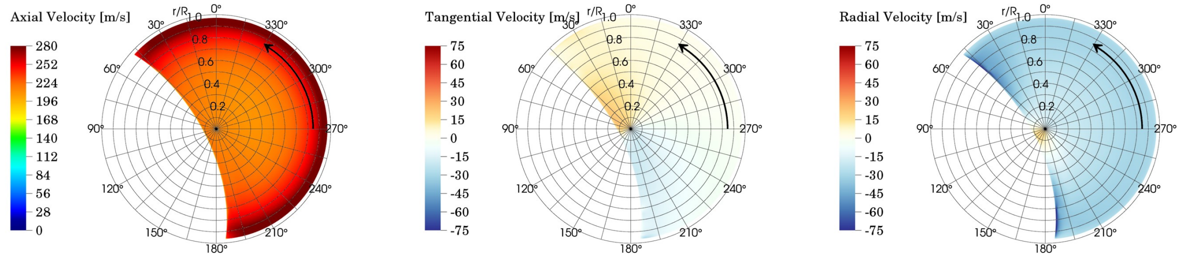

(a) *Axial component - x/R = -1.95* (b) *Tangential component - x/R = -1.95* (c) *Radial component - x/R = -1.95*

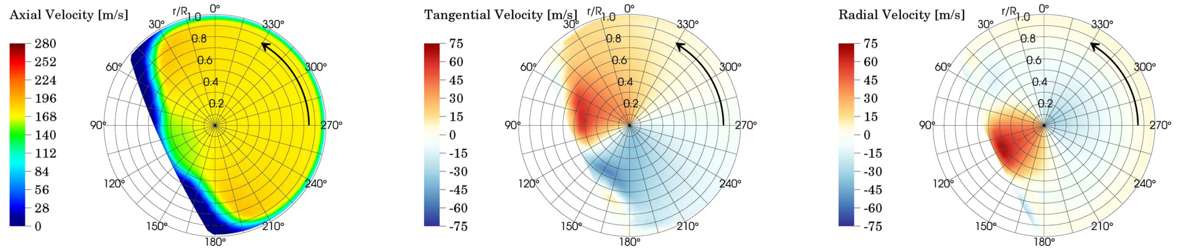

(d) *Axial component - x/R = -1.05* (e) *Tangential component - x/R = -1.05* (f) *Radial component - x/R = -1.05*

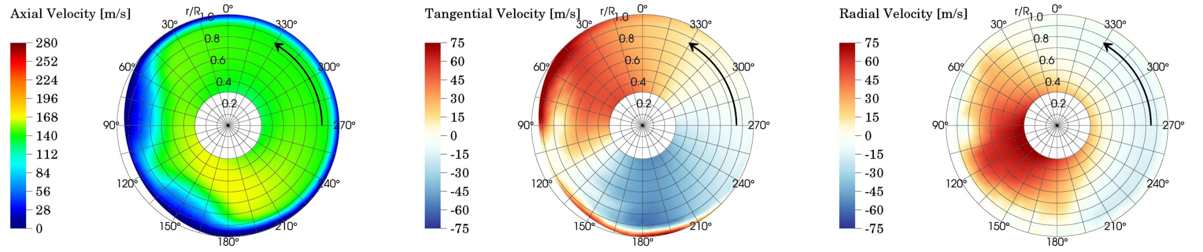

(g) *Axial component - x/R = -0.37* (h) *Tangential component - x/R = -0.37* (i) *Radial component - x/R = -0.37*

Figure 8. Time-averaged velocity field at different section upstream the fan, BLI engine.

Regarding the BLI configuration, the reduced engine inlet frontal area yields to an increase of the axial (Fig. 8(a)) and inward radial (Fig. 8(c)) velocity components compared to the isolated case. For further downstream sections, the mean flow exhibits high levels of non-uniformity and distortion in terms of axial, tangential and radial velocities. More specifically, the axial component shows two nearly symmetric recirculation/low-velocity regions on the fuselage side. Such flow separation areas are already visible at 55% of the intake extension (Fig. 8(d)) and extend further downstream (Fig. 8(g)) according to a nearly symmetrical pattern around the intake plane of symmetry of the installed configuration (120° in the fan blade azimuth). A nearly symmetrical pattern around 120° of the fan blade azimuth is also observable for the tangential (Figs. 8(e) and 8(h)) and radial velocities (Figs. 8(f) and 8(i)), with both velocity fields indicating an in-plane secondary flow motion directed towards the divergent s-duct wall on the fuselage side. Finally, it is interesting to highlight the entrainment motion imparted by the rotor blades when the low-velocity flow approaching the fan face for $r/R > 0.9$ and azimuthal angles within 45°-90° and 135°-210°, respectively (Fig. 8(h)).

IV.B.2. Interstage Flow Field

In order to obtain a better understanding of BLI installation effects on rotor/stator interaction mechanisms, Figs. 9 and 10 show upstream-looking-downstream views of the velocity field for an interstage section located at mid-distance between the rotor and the stator for the BLI and isolated configurations, respectively. More specifically, the velocity field is decomposed into phase-locked average of axial (Figs. 9(a) and 10(a)), tangential (Figs. 9(b) and 10(b)) and radial (Figs. 9(c) and 10(c)) velocity components, and standard deviation of axial (Figs. 9(d) and 10(d)) and in-plane (Figs. 9(e) and 10(e)) velocity components. It is worth mentioning that the phase-locked average contour plots highlight the presence of periodic non-uniformities in the mean flow associated to the rotating fan blades (i.e. viscous blade wakes and tip-vortices), which generate tonal noise at BPF and its harmonics when they interact with the stator vanes. Instead, the phase-locked standard deviation contour plots can be used to examine the presence of random fluctuations in the flow (i.e. turbulence), which represent potential sources of broadband noise when they impinge on the stator surfaces.

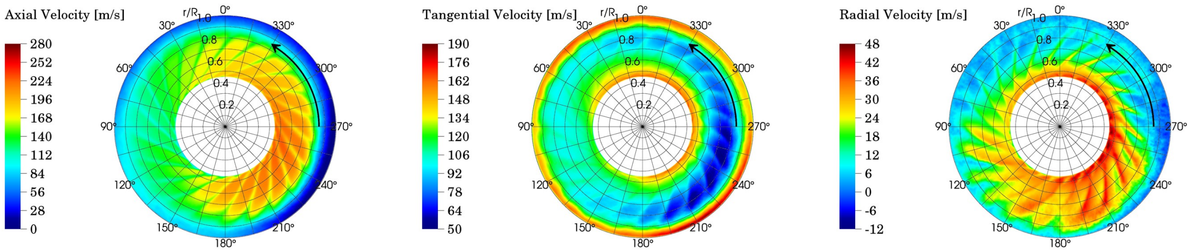

(a) *Axial component - x/R = 0.36* (b) *Tangential component - x/R = 0.36* (c) *Radial component - x/R = 0.36*

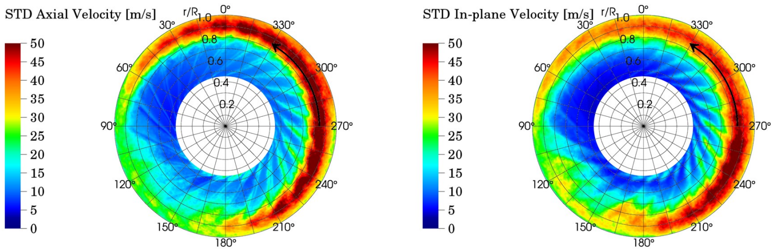

(d) *Axial component - x/R = 0.36* (e) *In-plane component - x/R = 0.36*

Figure 9. Phase-locked average of axial (a), tangential (b) and radial (c) velocity components and standard deviation (STD) of axial (d) and in-plane (e) velocity components on an interstage disk at x/R = 0.36, BLI engine.

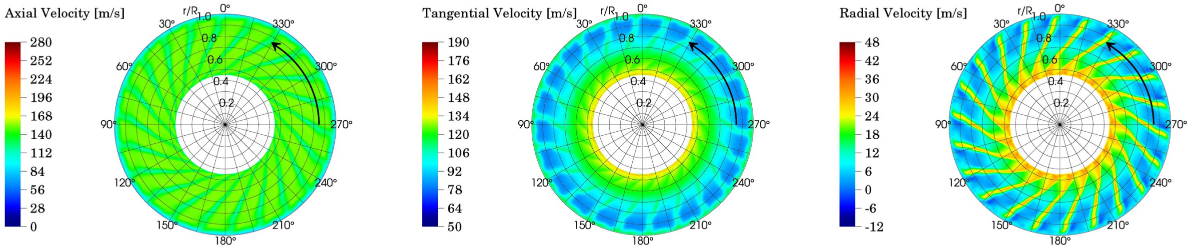

(a) *Axial component - x/R = 0.36* (b) *Tangential component - x/R = 0.36* (c) *Radial component - x/R = 0.36*

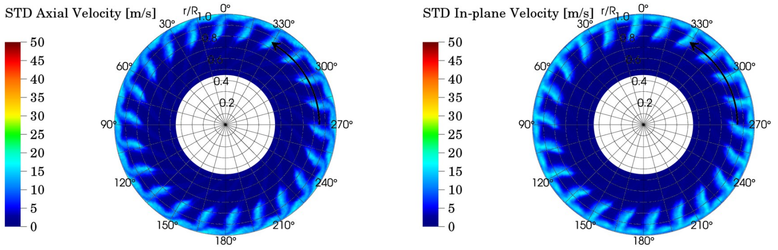

(d) *Axial component - x/R = 0.36* (e) *In-plane component - x/R = 0.36*

Figure 10. Phase-locked average os axial (a), tangential (b) and radial (c) velocity components and standard deviation (STD) of axial (d) and in-plane (e) velocity components on an interstage disk at x/R = 0.36, isolated engine.

Contrarily to the isolated configuration, where the two typical expected flow regions downstream the fan, i.e. the viscous region associated to both rotor blade wakes and tip-vortices and the potential flow region comprising the passage flow outside the viscous ones, are clearly defined throughout the radial coordinate (Figs. 10(a) to 10(c)), the same regions are visible only up to 80% of the span-wise coordinate for the BLI case (Figs. 9(a) to 9(c)). For the isolated configuration, the axial velocity in the potential flow regions is quite uniform (Fig. 10(a)) along the span-wise direction, whereas the tangential (Fig. 10(b)) and radial (Fig. 10(c)) ones tend to decrease as the radius increases. Moreover, for a given radial position, the axial velocity is lower in the viscous regions of the flow compared to the potential ones, whereas both tangential and radial ones result to be higher. Similar trends can also be found for the BLI configuration, although some additional considerations need to be outlined. First, the phase-locked averaged axial velocity shows non-uniform values along the azimuthal coordinate, with higher values within 0°-45° and 135°-360° and lower values in the explementary circular sector compared to the isolated case. The same trend also occurs for the tangential component within the first 55% of the radial coordinate, whereas an opposite situation is observed for $0.55 < r/R < 0.85$. Moreover, the flow presents lower axial velocities and higher tangential velocities above $r/R = 0.8$ compared to the isolated case. Finally, the radial component shows higher values in both viscous and potential regions throughout the azimuthal coordinate for inboard positions and for azimuthal angles between roughly 90°-270° for outboard ones.

Regarding the turbulent fluctuations, the isolated case shows quite uniform standard deviation contours, with the largest velocity perturbations occurring within the viscous wake and at the tip for both axial (Fig. 10(d)) and in-plane velocity components (Fig. 10(e)). Contrarily, the BLI configuration shows larger levels of fluctuations and flow non-uniformity for both components (Figs. 9(d) and 9(e), respectively). More specifically, velocity fluctuations roughly three times higher are observed within the outer 30% of the radial coordinate and for azimuthal position comprised between 0°-60° and 180°-360°, respectively. A secondary diffused region of high turbulence levels is also present between 50°-180°, i.e. in correspondence of the fuselage BLI area. Moreover, thicker viscous wakes are observed for the BLI configuration compared to the isolated one, especially for azimuthal angle between 180° and 360°.

Overall, the BLI interstage flow field is characterized by less periodic and coherent mean flow tangential velocity and higher levels of random in-plane velocity fluctuations. It is worth mentioning that such velocity components are thought to be more important in the generation of the rotor/stator interaction noise. This type of noise is associated to the unsteady loading on the stator vanes, which is generated by fluctuations of the flow velocity component normal to the stator surface. In view of this, broadband noise is expected to dominate more the far-field noise spectrum for the installed configuration compared to the isolated case.

IV.C. Fan Blade Sectional Air-loads

Figure 11 depicts the $c_x\tilde{U}^2$ coefficient time history (where c_x is the section axial force coefficient resulting only from the air-foil pressure distribution, and $\tilde{U} = u/a_\infty$ is the local fan blade section velocity u normalized by the free-stream speed of sound a_∞) at the six different span-wise sections uniformly distributed between 45% and 95% of the blade span. It should be noted that a negative value of the $c_x\tilde{U}^2$ coefficient has hereby the meaning of positive thrust. The isolated configuration shows almost constant time histories of the sectional thrust for each span-wise location, with a mean value increment moving from inboard (Fig. 11(a)) to outboard (Fig. 11(f)) sections of the fan blade. Only the outer section at $r/R = 0.95$ shows some weak unsteadiness due to the interaction between the blade tip and the boundary layer convecting along the intake wall. Contrarily, the BLI configuration shows a low-frequency thrust unsteadiness (predominantly 1/rev) for inboard blade sections (Figs. 11(a) to 11(c)), as a consequence of the strong mean flow distortion. For these sections, an increment of the section thrust is observed approximately between 60° and 180° compared to the isolated case, whereas lower values of the $c_x\tilde{U}^2$ coefficient are observed elsewhere. As the radial coordinate increases, more intense and impulsive unsteadiness, as well as lower mean values of the section thrust are observed (Figs. 11(d) to 11(f)) compared to the isolated case, as a result of the ingestion of turbulence associated to the flow separation on both fuselage and nacelle sides. All the aforementioned thrust fluctuations represent an additional source of noise. Among them, those occurring on the outer part of the blade are expected to contribute more to the far-field noise, due to the higher levels of unsteadiness and higher Mach numbers compared to blade inboard regions.

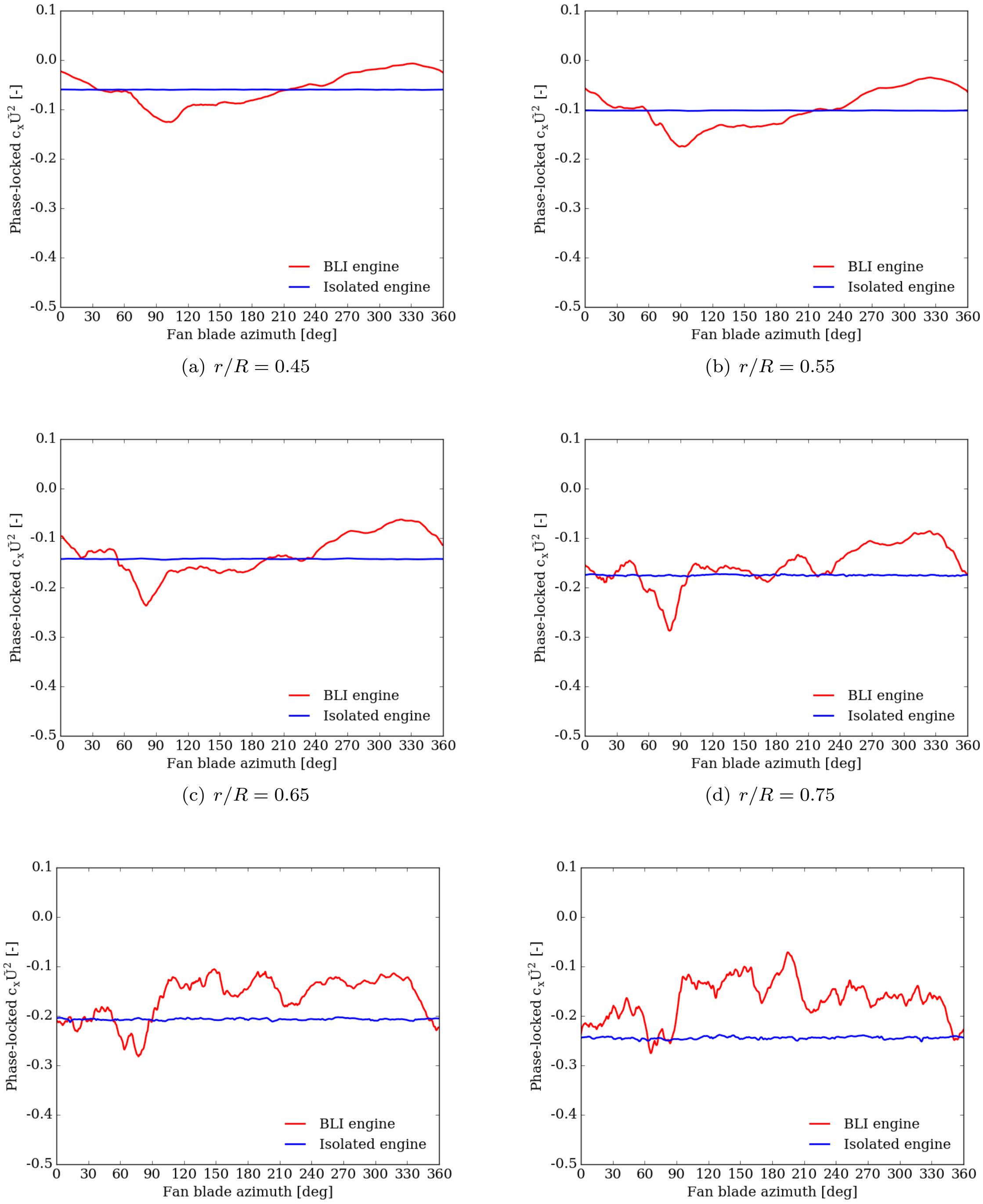

(a) $r/R = 0.45$

(b) $r/R = 0.55$

(c) $r/R = 0.65$

(d) $r/R = 0.75$

(e) $r/R = 0.85$

(f) $r/R = 0.95$

Figure 11. Phase-locked fan blade axial force component coefficient time histories at different span-wise locations.

IV.D. Noise directivity

Figure 12 depicts the microphone array used in this study for far-field noise computations. It is composed by 7 even meridian arcs of 10 m radius, centered around the fan center and covering a semi-spherical surface. Each arc is characterized by 15 microphones distributed every 10°, from 20° upstream the engine to 160° downstream it. As mentioned in Sec. III.B, the far-field noise is computed by integration of the FW-H equation on a permeable surface encompassing the engine. Since the FW-H formulation adopted does not include the volume integral, spurious signals might arise when the permeable surface is intersected by turbulence (i.e. the fuselage turbulent boundary layer).[39] The presence of such spurious effects has been assessed (for the BLI case) by comparing far-field noise predictions from the whole permeable FW-H surface to those obtained by removing that portion of the surface being intersected by the fuselage boundary layer (depicted in dark orange in Fig. 2). It turned out that the two different approaches provided almost identical results within the directivity angles of interest, thus allowing the use of the whole FW-H permeable surface (even for the BLI configuration) for far-field noise computations.

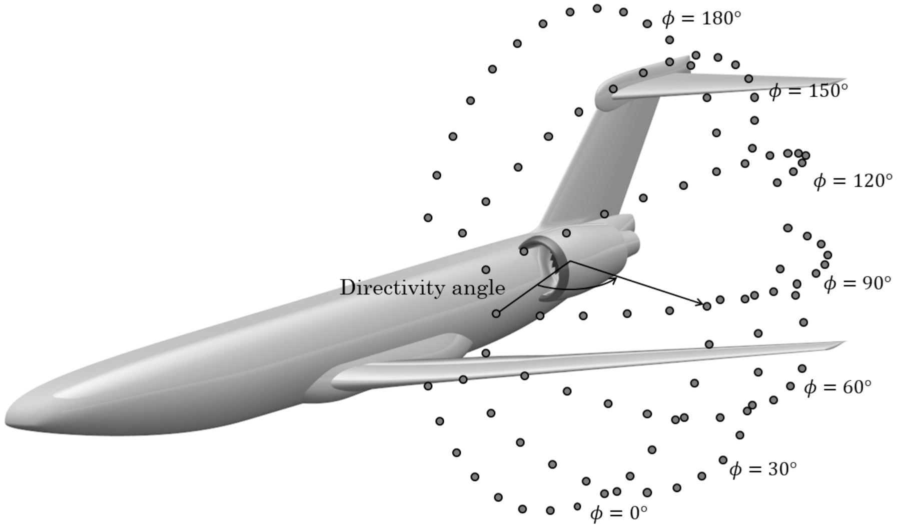

Figure 12. Schematic description of the microphone array used for far-field noise computations. The angle ϕ denotes the azimuthal coordinate used to define each arc position.

A spectral representation (Power Spectral Density, PSD) of the far-field noise directivity normalized by the BPF is shown in Fig. 13 and Fig. 14 for the BLI and isolated cases, respectively. In addition, far-field noise differences between such configurations are depicted in Fig. 15. For the sake of conciseness, only the results for the arcs at $\phi = 0°$, $30°$, $60°$ and $90°$ are shown in following, being them the most interesting ones from an on-the-ground noise radiation viewpoint. For both BLI and isolated configurations, noise is radiated most efficiently downstream the engine. However, besides such a similarity, the two examined configurations show quite different results. The isolated engine presents both broadband and tonal noise contributions, with the latter showing distinct peaks at multiples of the blade-passing frequency downstream the engine (up to BPF-3). Conversely, tones at harmonics of the BPF are not clearly emerging with respect to broadband levels for the BLI case. However, haystacked peaks are found around BPF-1 for downstream observer angles. Such peaks are believed to be generated by the correlated unsteady air-loads on neighboring blades, and associated to the large eddies being shed from the s-duct wall and cut multiple times by successive blades (a similar phenomenon has been already observed by Alexander *et al*[40] and Murray *et al*[20] for a rotor case ingesting a planar boundary layer). For the BLI case, broadband levels turn out to be from 10 to 20 dB overall higher than those related to the isolated configuration, for most of the frequencies and directivity angles considered. Moreover, the BLI layout appears to be as noisy as the isolated one along the sideline direction (i.e. for directivity angles around 90°) and frequencies higher than BPF-2 (Figs. 15(c) and 15(d)), or quieter by 5-10 dB for those meridian arcs facing the ground (Figs. 15(a) and 15(b)). This last point might be related to some noise shielding effects introduced by the partial placement of the engine into the fuselage.

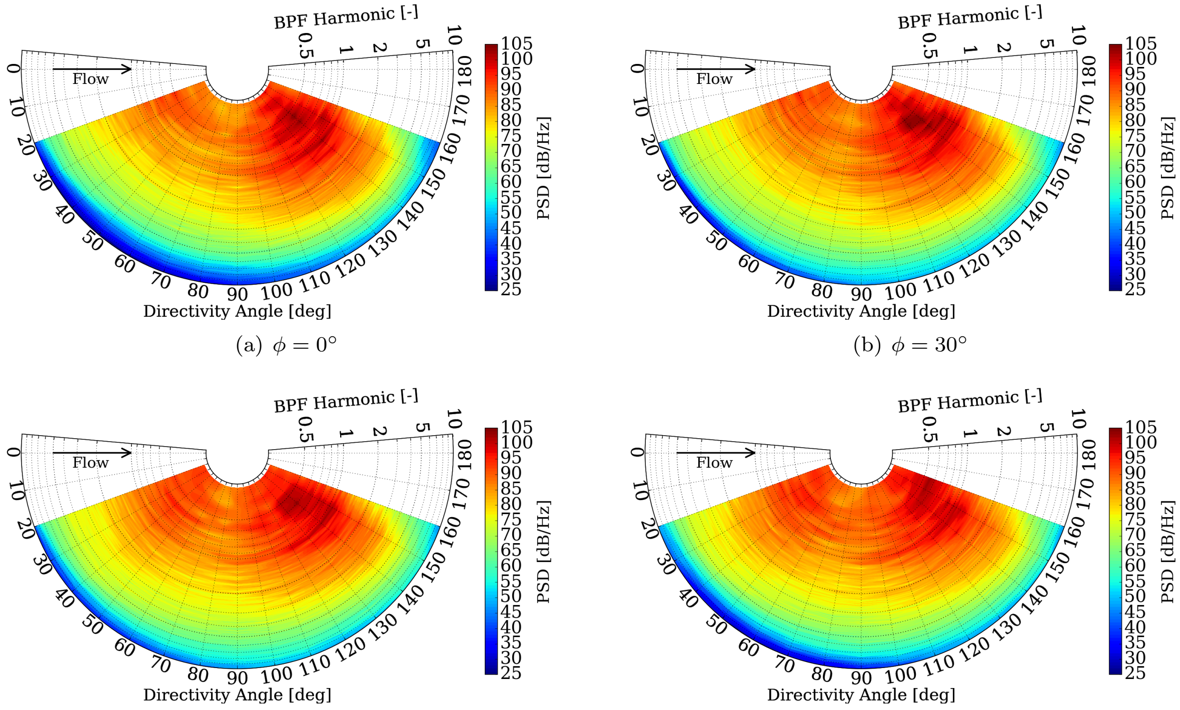

(a) $\phi = 0°$

(b) $\phi = 30°$

(c) $\phi = 60°$

(d) $\phi = 90°$

Figure 13. Far-field noise directivity on circular array of 10 m radius centered around the fan for different azimuthal locations, BLI engine.

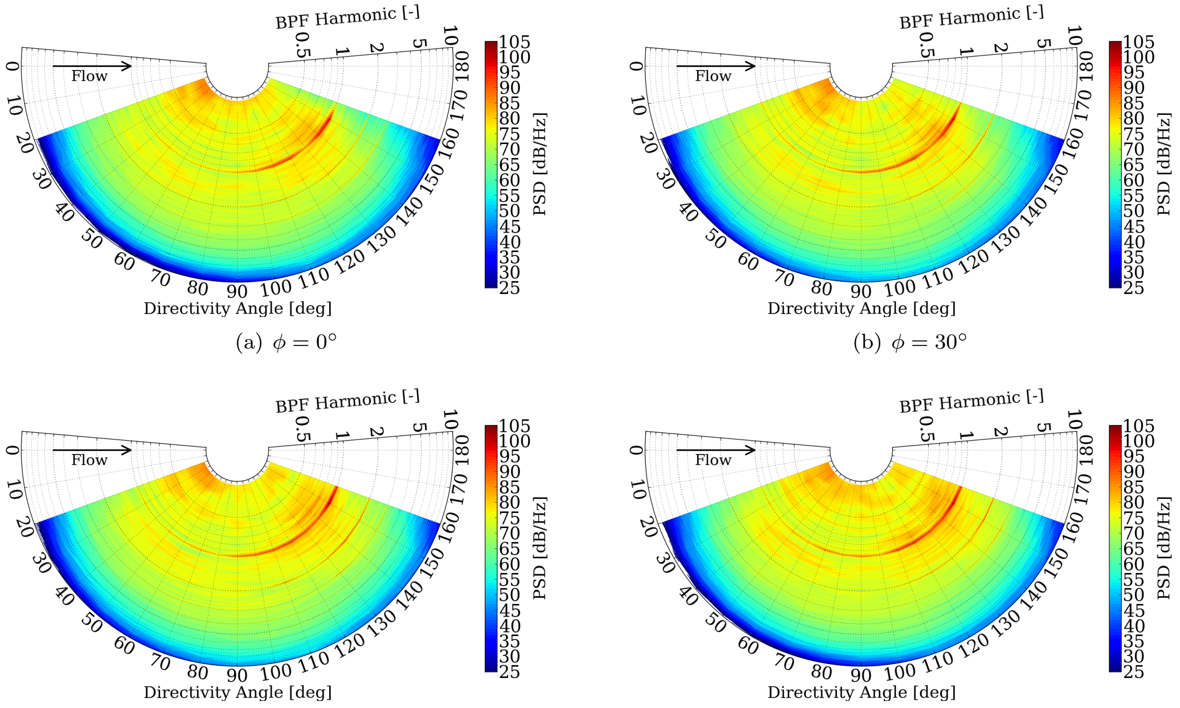

(a) $\phi = 0°$

(b) $\phi = 30°$

(c) $\phi = 60°$

(d) $\phi = 90°$

Figure 14. Far-field noise directivity on circular array of 10 m radius centered around the fan for different azimuthal locations, isolated engine.

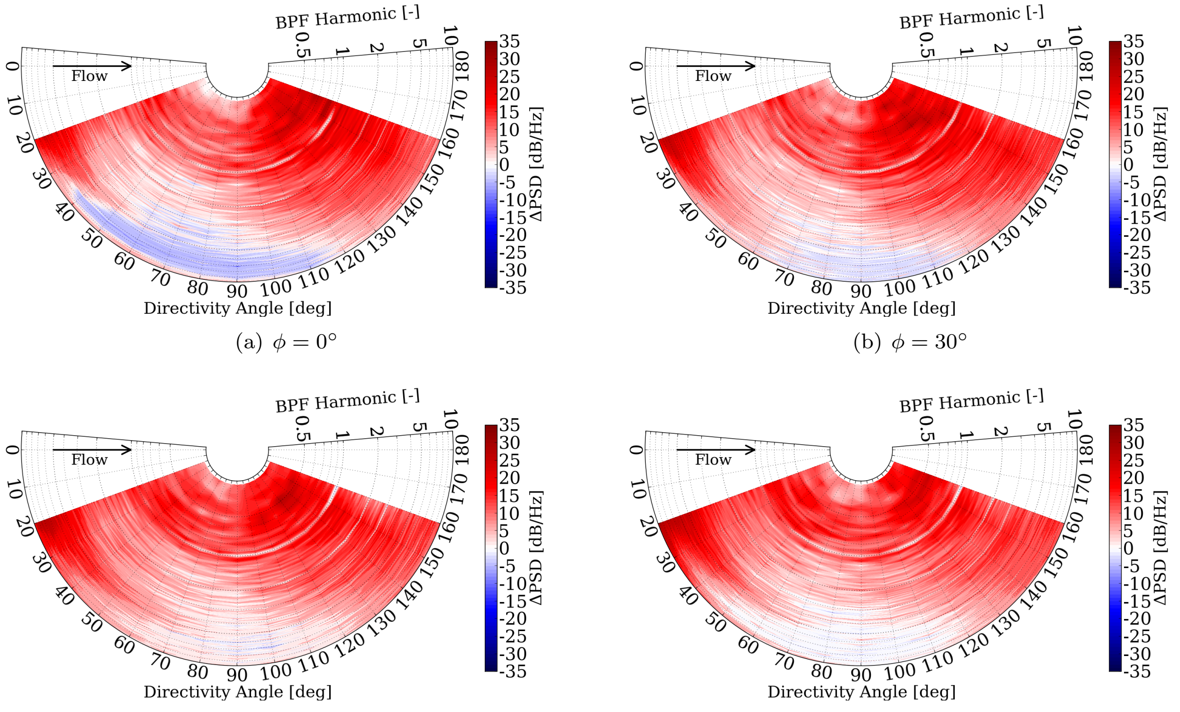

(a) $\phi = 0°$ (b) $\phi = 30°$

(c) $\phi = 60°$ (d) $\phi = 90°$

Figure 15. Far-field noise directivity on circular array of 10 m radius centered around the fan for different azimuthal locations, difference between BLI and isolated engines.

IV.E. Noise Power Levels

To conclude the analysis on fan noise installation effects, in Fig. 16 one-side narrow-band source Power Level (PWL) is presented for both BLI (Fig. 16(a)) and isolated (Fig. 16(b)) configuration. For convenience, the difference between the power levels of the two cases is also shown in Fig. 16(c). In this study, the PWL is computed by integration of the PSDs over the semi-spherical surface portion corresponding to the aforementioned microphone array, using the following formula:

$$\mathrm{PWL}(f) = \int_{\theta_{min}}^{\theta_{max}} \int_{\phi_{min}}^{\phi_{max}} R^2 \sin(\theta) \frac{[1 + M_\infty \cos(\theta)]^2 \mathrm{PSD}(f,\theta)}{2\rho_\infty a_\infty} d\phi d\theta \tag{4}$$

where f is the frequency, R is the semi-sphere radius, ϕ is the azimuthal angle (defined as in Fig. 12) and varying from $\phi_{min} = 0°$ to $\phi_{max} = 180°$, whereas θ is the directivity angle varying from $\theta_{min} = 20°$ to $\theta_{max} = 160°$. Moreover, M_∞ is the free-stream Mach number, and ρ_∞ and a_∞ are the ambient density and speed of sound, respectively.

As already observed, broadband levels dominate the power level spectrum for the BLI configuration, as consequence of the less coherent rotor wakes and higher levels of turbulence impinging the stator vanes. No tones at harmonics of the BPF are observed, and only a weak haystacked peak around BPF-1 is found. As mentioned before, this broadband peak might be connected to some blade-to-blade unsteady air-loads correlation associated to the simultaneous impingement of large vortical structures separating from the s-duct wall, with multiple neighboring fan blades. Finally, regarding the isolated engine, the PWL presents distinct tones at the first 3 blade-passing frequencies, and much lower broadband source power levels, from 4-5 dB at high frequencies up to 15-18 dB at low ones, with respect to the BLI configuration.

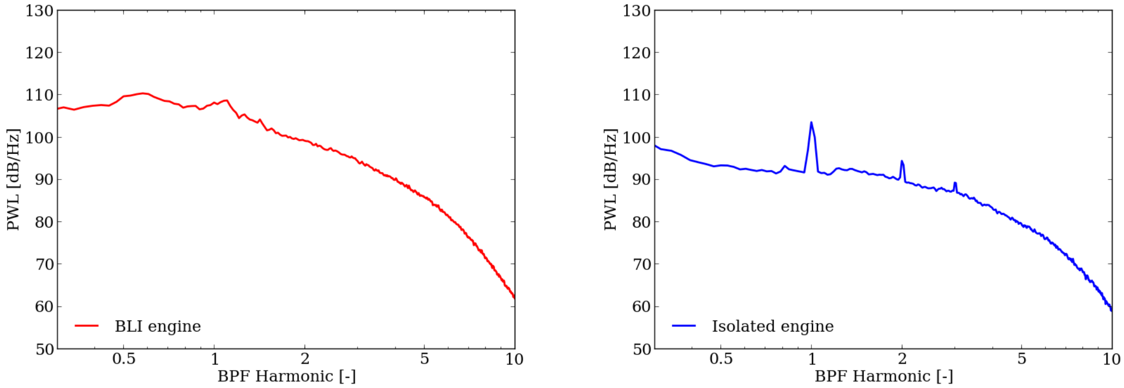

(a) *BLI engine* (b) *Isolated engine*

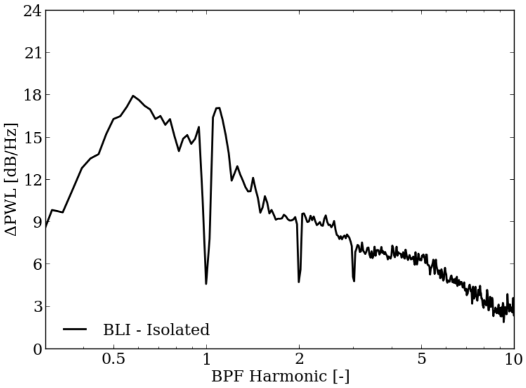

(c) *BLI - isolated engine*

Figure 16. Source Power Level: BLI engine (a), isolated engine (b) and difference between BLI and isolated engines (c).

V. Conclusions and Future Outlook

For the first time, a high-fidelity CFD/CAA simulation of a full-scale aircraft geometry comprehensive of a BLI fan/OGV stage was performed. A modified version of the Low-Noise configuration of the NASA SDT fan-stage was embedded into the ONERA NOVA fuselage in order to reproduce the NOVA BLI aircraft configuration. The numerical flow solution was obtained by solving the explicit, transient and compressible lattice-Boltzmann equation implemented in the high-fidelity CFD/CAA solver Simulia PowerFLOW®. The acoustic far-field was computed by using the Ffwocs-Williams & Hawkings integral solution applied to a permeable surface encompassing the fan-stage. Fuselage BLI installation effects were investigated by comparison with an isolated setup of the modified Low-Noise SDT fan-stage geometry in terms of intake and interstage velocity fields, fan blade unsteady air-loads and far-field noise. All simulations were performed for an operating condition representative of a take-off with power cutback.

The analysis of the fan-stage velocity field showed that, for the considered operating condition and geometry, the embedded BLI fan-stage causes high levels of mean flow distortion and flow separation at approximately 60% of the s-duct length and in proximity of the fan plane on the nacelle side. The mean flow distortion was found to be responsible of a low-frequency periodic variation of the fan blade section thrust for inboard blade sections. The ingestion of turbulence, associated to the flow separation on the s-duct and intake walls, led to high levels of unsteadiness, as well as to a deficit in thrust generation in outboard blade regions. In addition, the BLI engine interstage flow field was characterized by less periodic and coherent tangential velocity variations associated to the rotor wake, and higher levels of in-plane velocity fluctuations, compared to the isolated engine configuration.

Far-field noise directivity predictions revealed that the noise is radiated most efficiently downstream the engine for the BLI layout, as also observed for the isolated engine. However, while the latter manifested both broadband and tonal noise contributions, no tones clearly emerged with respect to broadband levels for the BLI case. Weak haystacked peaks ware found around BPF-1 for downstream observer angles. Such peaks might be connected to some blade-to-blade unsteady air-loads correlation associated to the simultaneous impingement of large vortical structures separating from the s-duct wall with multiple neighboring fan blades. Overall, the BLI configuration showed from 10 to 20 dB higher broadband levels in the far-field compared those related to the isolated configuration, for most of the frequencies and directivity angles considered. The BLI layout resulted to be as noisy as the isolated one, or quieter by 5-10 dB for meridian arcs facing the ground due to some fuselage shielding, only for directions nearly perpendicular to the engine axis and for frequencies higher than BPF-2.

As future outlook, simulations by employing flow-control techniques will be performed for the BLI configuration in order to mitigate the flow separation over the s-duct wall and the related benefits in terms of noise emission will be assessed.

Acknowledgments

This project has received funding from the European Union's Horizon 2020 research and innovation programme under grant No 769 350. The authors would further like to thank the Department of Aerodynamics, Aeroelasticity and Aeroacoustics of ONERA for the provision of the NOVA fuselage geometry, with wing and empennage, that was used in this study.

References

[1] Kallas, S., Geoghegan-Quinn, M., Darecki, M., Edelstenne, C., Enders, T., Fernandez, E., and Hartman, P., "Flightpath 2050 Europe's Vision for Aviation," *Report of the High Level Group on Aviation Research, European Commission, Brussels, Belgium, Report No. EUR*, Vol. 98, 2011.

[2] Hughes, C. E., "NASA Collaborative Research on the Ultra High Bypass Engine Cycle and Potential Benefits for Noise, Performance, and Emissions," *Technical Memorandum TM-2013-216345, NASA*, 2013.

[3] Greitzer, E. M., Bonnefoy, P., De la Rosa Blanco, E., Dorbian, C., Drela, M., Hall, D., Hansman, R., Hileman, J., Liebeck, R., Levegren, J., et al., "N+ 3 Aircraft Concept Designs and Trade Studies. Volume 1," *Nasa CR-2010-216794/vol2, NASA Gleen Research Center Cleveland, Ohio*, 2010.

[4] Heykena, C., Savoni, L., Friedrichs, J., and Rudnik, R., "Engine Airframe Integration Sensitivities For a STOL Commercial Aircraft Concept with over-the-wing Mounted UHBR-Turbofans," *Proceedings of Montreal 2018 Global Power and Propulsion Forum*, 2018.

[5] Wiart, L., Atinault, O., Grenon, R., Paluch, B., and Hue, D., "Development of NOVA Aircraft Configurations for Large Engine Integration Studies," *33rd AIAA Applied Aerodynamics Conference*, 2015, p. 2254.

[6] Wiart, L., Atinault, O., Boniface, J.-C., and Barrier, R., "Aeropropulsive Performance Analysis of the NOVA Configurations," *30th Congress of the International Council of the Aerodynamical Sciences*, 2016.

[7] Plas, A., Crichton, D., Sargeant, M., Hynes, T., Greitzer, E., Hall, C., and Madani, V., "Performance of a Boundary Layer Ingesting (BLI) Propulsion System," *45th AIAA aerospace sciences meeting and exhibit*, 2007, p. 450.

[8] Drela, M., "Power Balance in Aerodynamic Flows," *AIAA journal*, Vol. 47, No. 7, 2009, pp. 1761–1771.

[9] Hardin, L., Tillman, G., Sharma, O., Berton, J., and Arend, D., "Aircraft System Study of Boundary Layer Ingesting Propulsion," *48th AIAA/ASME/SAE/ASEE Joint Propulsion Conference & Exhibit*, 2012, p. 3993.

[10] Carrier, G., Atinault, O., Grenon, R., and Verbecke, C., "Numerical and Experimental Aerodynamic Investigations of Boundary Layer Ingestion for Improving Propulsion Efficiency of Future Air Transport," *31st AIAA Applied Aerodynamics Conference*, 2013, p. 2406.

[11] Sabo, K. M. and Drela, M., "Benefits of Boundary Layer Ingestion Propulsion," *53rd AIAA Aerospace Sciences Meeting*, 2015, p. 1667.

[12] Lv, P., Ragni, D., Hartuc, T., Veldhuis, L., and Rao, A., "Experimental Investigation of the Flow Mechanisms Associated with a Wake-ingesting Propulsor," *AIAA Journal*, 2016, pp. 1332–1342.

[13] Lv, P., Rao, A. G., Ragni, D., and Veldhuis, L., "Performance Analysis of Wake and Boundary-Layer Ingestion for Aircraft Design," *Journal of Aircraft*, Vol. 53, No. 5, 2016, pp. 1517–1526.

[14] Uranga, A., Drela, M., Greitzer, E. M., Hall, D. K., Titchener, N. A., Lieu, M. K., Siu, N. M., Casses, C., Huang, A. C., Gatlin, G. M., et al., "Boundary Layer Ingestion Benefit of the D8 Transport Aircraft," *AIAA Journal*, 2017, pp. 3693–3708.

[15] Anabtawi, A., Blackwelder, R., Lissaman, P., and Liebeck, R., "An Experimental Investigation of Boundary Layer Ingestion in a Diffusing S-duct with and without Passive Flow Control," *37th Aerospace Sciences Meeting and Exhibit*, 1999, p. 739.

[16] Gorton, S., Owens, L., Jenkins, L., Allan, B., and Schuster, E., "Active Flow Control on a Boundary-layer-ingesting Inlet," *42nd AIAA Aerospace Sciences Meeting and Exhibit*, 2004, p. 1203.

[17] Owens, L. R., Allan, B. G., and Gorton, S. A., "Boundary-layer-ingesting Inlet Flow Control," *Journal of Aircraft*, Vol. 45, No. 4, 2008, pp. 1431–1440.

[18] Defoe, J. J. and Spakovszky, Z. S., "Effects of Boundary-Layer Ingestion on the Aero-Acoustics of Transonic Fan Rotors," *Journal of Turbomachinery*, Vol. 135, No. 5, 2013, pp. 051013.

[19] Clark, I., Thomas, R. H., and Guo, Y., "Aircraft System Noise Assessment of the NASA D8 Subsonic Transport Concept," *2018 AIAA/CEAS Aeroacoustics Conference*, 2018, p. 3124.

[20] Murray, H. H., Devenport, W. J., Alexander, W. N., Glegg, S. A., and Wisda, D., "Aeroacoustics of a Rotor Ingesting a Planar Boundary Layer at High Thrust," *Journal of Fluid Mechanics*, Vol. 850, 2018, pp. 212–245.

[21] Casalino, D., Hazir, A., and Mann, A., "Turbofan Broadband Noise Prediction using the Lattice Boltzmann Method," *AIAA Journal*, Vol. 56, No. 2, 2017, pp. 609–628.

[22] Casalino, D., Hazir, A., and Mann, A., "Turbofan Broadband Noise Prediction using the Lattice Boltzmann Method," *AIAA Journal*, Vol. 56, 2018, pp. 609–628.

[23] Gonzalez-Martino, I. and Casalino, D., "Fan Tonal and Broadband Noise Simulations at Transonic Operating Conditions Using Lattice-Boltzmann Methods," *2018 AIAA/CEAS Aeroacoustics Conference*, 2018, p. 3919.

[24] Envia, E., "Fan Noise Source Diagnostic Test-Vane Unsteady Pressure Results," *AIAA Paper 2002-2430*, 2002.

[25] Nie, X., Shan, X., and Chen, H., "A Lattice-Boltzmann/Finite-Difference Hybrid Simulation of Transonic Flow," *AIAA Paper 2009-0139*, 2009.

[26] Chen, H., Chen, S., and Matthaeus, W., "Recovery of the Navier-Stokes Equations Using a Lattice-Gas Boltzmann Method," *Physical Review A*, Vol. 45, No. 8, 1992, pp. 5339–5342.

[27] Bhatnagar, P. L., Gross, E. P., and Krook, M., "A Model for Collision Processes in Gases. I. Small Amplitude Processes in Charged and Neutral One-Component Systems," *Physical Review*, Vol. 94, No. 3, 1954, pp. 511–525.

[28] Chen, H., Teixeira, C. M., and Molvig, K., "Digital physics approach to computational fluid dynamics: some basic theoretical features," *International Journal of Modern Physics C*, Vol. 8, No. 4, 1997, pp. 675–684.

[29] Chen, H., Kandasamy, S., Orszag, S. A., Succi, S., and Yakhot, V., "Extended Boltzmann Kinetic Equation for Turbulent Flows," *Science*, Vol. 301, No. 5633, 2003, pp. 633–636.

[30] Yakhot, V. and Orszag, S. A., "Renormalization Group Analysis of Turbulence. I. Basic Theory," *Journal of Scientific Computing*, Vol. 1, No. 1, 1986, pp. 3–51.

[31] Yakhot, V., Orszag, S. A., Thangam, S., Gatski, T. B., and Speziale, C. G., "Development of Turbulence Models for Shear Flows by a Double Expansion Technique," *Physics of Fluids A*, Vol. 4, No. 7, 1992, pp. 1510–1520.

[32] Teixeira, C. M., "Incorporating Turbulence Models into the Lattice-Boltzmann Method," *International Journal of Modern Physics C*, Vol. 9, 1998, pp. 1159–1175.

[33] Alexander, C. G., Chen, H., Kandasamy, S., Shock, R., and Govindappa, S. R., "Simulations of Engineering Thermal Turbulent Flows Using a Lattice Boltzmann Based Algorithm," *ASME-PUBLICATIONS-PVP*, Vol. 424, 2001, pp. 115–126.

[34] Launder, B. E. and Spalding, D. B., "The Numerical Computation of Turbulent Flows," *Computer Methods in Applied Mechanics and Engineering*, Vol. 3, 1974, pp. 269–269.

[35] Chen, H., Teixeira, C., and Molvig, K., "Realization of Fluid Boundary Conditions via Discrete Boltzmann Dynamics," *International Journal of Modern Physics C*, Vol. 9, No. 8, 1998, pp. 1281–1292.

[36] Casalino, D., "An Advanced Time Approach for Acoustic Analogy Predictions," *Journal of Sound and Vibration*, Vol. 261, No. 4, 2003, pp. 583–612.

[37] Farassat, F. and Succi, G. P., "The Prediction of Helicopter Discrete Frequency Noise," *Vertica*, Vol. 7, No. 4, 1983, pp. 309–320.

[38] van der Velden, W., van Zuijlen, A., de Jong, A., and Ragni, D., "Flow and Self-noise Around Bypass Transition Strips," *Noise Control Engineering Journal*, Vol. 65, No. 5, 2017, pp. 434–445.

[39] Lopes, L. V., Boyd Jr, D. D., Nark, D. M., and Wiedemann, K. E., "Identification of Spurious Signals from Permeable Ffowcs Williams and Hawkings Surfaces," 2017.

[40] Alexander, W. N., Devenport, W. J., and Glegg, S. A., "Noise from a Rotor Ingesting a Tthick Boundary Layer and Relation to Measurements of Ingested Turbulence," *Journal of Sound and Vibration*, Vol. 409, 2017, pp. 227–240.